ARTICLE

Rapid Hybrid Chemical Vapor Deposition for Efficient and Hysteresis-Free Perovskite Solar Modules with Operation Lifetime Exceeding 800 Hours

Received 00th January 20xx,
Accepted 00th January 20xx

DOI: 10.1039/x0xx00000x

Longbin Qiu,† Sisi He,† Zonghao Liu, Luis K. Ono, Dae-Yong Son, Yuqiang Liu, Guoqing Tong, Yabing Qi*

Hybrid chemical vapor deposition (HCVD) has been employed in fabrication of perovskite solar cells (PSCs) and modules (PSMs), which shows promise in upscalable fabrication. However, the conventional HCVD process usually requires a relatively long processing time (e.g., several hours) and the PSCs often exhibit a salient hysteresis behavior, which impedes this technology to mass production. Herein, we demonstrate a rapid HCVD (RHCVD) fabrication process of PSCs using a rapid thermal process, which not only significantly reduces the deposition time to <10 min but also effectively suppresses hysteresis. This markedly reduced deposition time is comparable to solution coating processes. Furthermore, the shorter processing time inside the furnace reduces the exposure time of the glass/ITO/SnO_2 substrates in vacuum, which helps maintain the high quality of SnO_2 electron-transport layer resulting in a lower density of gap states. Finally, 22.4 cm^2 PSMs fabricated by RHCVD achieved an efficiency of 12.3%, and maintained 90% of the initial value after operation under continuous light illumination for over 800 h.

Introduction

Perovskite as a low-cost material is boosting the performance up to 25.2% for small area (0.09 cm^2) single-junction solar cells[1] and the expected levelized cost of electricity (LCOE) is as low as 3.5 US cents/kWh (as comparison, LCOE for grid power is 7.04 – 11.90 US cents/kWh and for c-Si solar cell is 9.78–19.33 US cents/kWh) when assuming a 1 m^2 module with 20% efficiency and >15 years lifetime[2-3], and this exceeds the 2030 goals of US Department of Energy of 5 US cents/kWh for residential solar power.[4] Recently, there have been more and more works focusing on upscalable fabrication of perovskite solar modules (PSMs) to transfer the desired performance from small area cells to large-area modules.[5] However, there is still a large gap between small area cells and large-area modules.[5] To achieve upscalable fabrication, a key indicator is the performance decay rate upon upscaling. For mature photovoltaic technologies (e.g., crystalline silicon solar cells, polycrystalline silicon solar cells, CdTe solar cells), the absolute performance decay rate is around 0.8%/decade area increase.[6-7] If the same decay rate can be realized for perovskite photovoltaic technologies, a power conversion efficiency (PCE) of approximately 22% would be expected for a module with the area of approximately 1000 cm^2 when scaling up from state of the art small area cells (25.2% PCE with a cell area of 0.0937 cm^2).[6] Currently the highest reported PCE for such a large-size PSM was 16.1% with a designated area of 802 cm^2.[1] To reduce the large PCE gap between small area cells and large-area modules, upscalable fabrication methods for perovskite and other functional layers (e.g., electron transport layer (ETL), hole transport layer (HTL), electrode and interface modification) are required.[5] For the upscalable fabrication of perovskite solar cells (PSCs), both solution- and vapor-based processes have been reported, including doctor blading,[8-9] slot-die coating,[10] spray coating,[11] thermal evaporation[12] and hybrid chemical vapor deposition (HCVD).[5, 13-14]

HCVD is a promising method as compared to the solution-based ones because of its advantages such as uniform deposition across large area, low cost, solvent-free, and readiness for integration with other thin film solar technologies (e.g., thin film silicon solar cells) to form tandem solar cells.[13] Currently, the decay rate between small area cells and large area modules upon upscaling is 1.3%/decade area increase,[15] which is approaching other mature photovoltaic technologies. HCVD is a two-step deposition process. In the first step, inorganic precursor materials (e.g., PbI_2, $PbCl_2$, CsI, etc.) is deposited by thermal evaporation,[14] spray coating[13] or spin coating.[16] In the second step, organic precursor materials (e.g., FAI, MAI, MABr, etc., where FA is formamidinium and MA is methylammonium) is sublimed in the first heating zone of a CVD tube furnace, and subsequently driven by a gas flow (e.g., N_2, Ar, or dry air) towards the second heating zone, where the organic precursor vapor reacts with the inorganic precursor that is pre-deposited on the substrate, leading to perovskite film growth.[14-15] Based

Energy Materials and Surface Sciences Unit (EMSSU), Okinawa Institute of Science and Technology Graduate University (OIST), 1919-1 Tancha, Kunigami-gun, Onna-son, Okinawa 904-0495, Japan.
* Corresponding Author: Yabing Qi, E-mail: Yabing.Qi@OIST.jp
† L. Qiu and S. He contributed equally to this work.
Electronic Supplementary Information (ESI) available.

on the pressure and zone temperatures, a variety of HCVD techniques can be developed to fabricate perovskite film including atmospheric pressure HCVD,[16-18] low-pressure HCVD,[14] single-zone HCVD[19-20] and double-zone HCVD.[14] However, all the HCVD processes usually take a relatively long processing time (2-3 hours), which severely limits mass-production capabilities for large-area solar cell fabrication. Reducing the deposition time is still a challenge that needs to be fully addressed for the further development of module-scale HCVD. Furthermore, it has been found that the longer deposition time has a detrimental effect on the ETL such as SnO_2 and TiO_2, which deteriorates the solar module performance.[15] Also, the hysteresis behaviour was observed for the un-optimized interface between this ETL layer and the perovskite layer. Incorporating an additional buffer layer such as C_{60} improves the HCVD processed solar cell performance by reducing the negative impact of vacuum annealing on ETL.[15] However, this additional layer increases the cost and complexity of the deposition process.

Herein, we report a rapid HCVD (RHCVD) process to fabricate PSCs and PSMs (**Figure 1**). The RHCVD process greatly reduced the deposition time from several hours to within 10 min, which is comparable with typical solution coating processes. As compared with the regular HCVD process, the RHCVD processed PSCs exhibited only slight hysteresis even without any additional interfacial buffer layer. Using RHCVD, we obtained an efficiency of 15.5% for small-area PSCs (active area = 0.1 cm^2). Furthermore, we show that the RHCVD process is readily upscalable and can be developed to fabricate PSMs, the area of which is only limited by the size of the CVD tube furnace. As a demonstration, we fabricated PSMs on 5 cm by 5 cm substrates with a designated area of 22.4 cm^2 and a geometric fill factor of approximately 90%. The performance of the PSMs is up to 12.3% with almost no hysteresis. The 224 times of increase of area with absolute PCE reduction of 2.9% (i.e., a decay rate of 1.2%/decade area) further confirms upscalability of this RHCVD technology. The operational lifetime of the encapsulated PSMs was tested under continuous light illumination with a steady voltage output (the initial maximum power point (MPP) voltage) and the module maintained 90% of its initial performance after operation for more than 800 h.

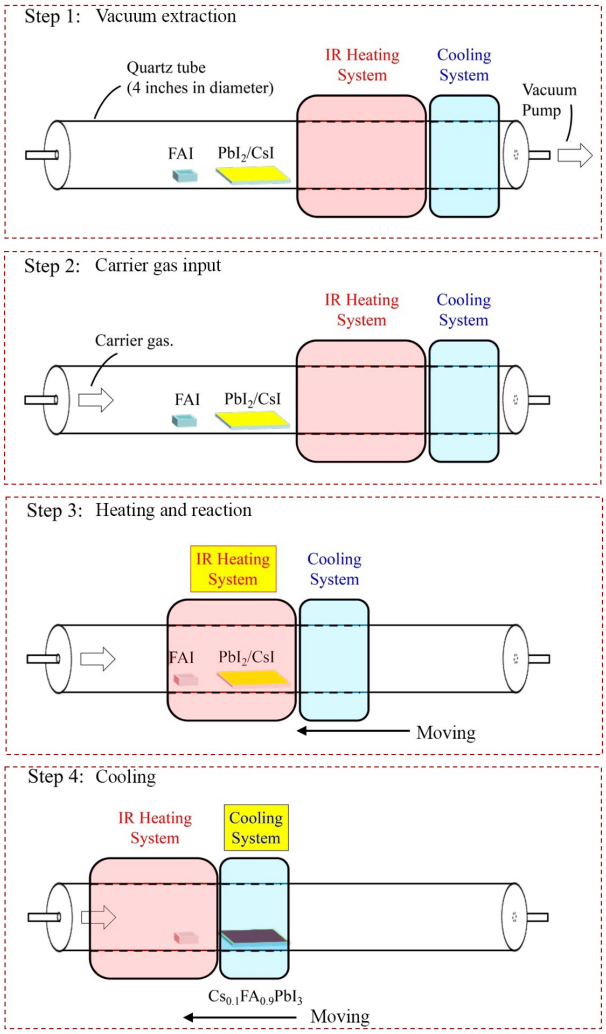

Figure 1. Schematic illustrations showing the steps and major features for fabricating perovskite films by the RHCVD method. **Step 1:** Loading of a crucible containing organic compound and solar module substrate(s) with the pre-coated inorganic layer into a single-zone quartz tube. **Step 2**: Flow of the carrier gas (e.g., N_2, Ar, air, etc) and keep the vacuum at 10 Torr. **Step 3**: Slide the IR Heating System to enclose both the organic powder and substrate and start of the IR Heating System. **Step 4**: After the heating process is finished, the IR Heating System is turned off and the Cooling System is turned on. The Cooling System is slided to the substrate position.

Results and discussion

In this work, we used an n-i-p planar PSC structure with the perovskite layer sandwiched between ETL and HTL, which is a simple structure without the use of mesoporous structures.[21] This structure also eliminates the high-temperature step needed to process mesoporous structures, which helps reduce cost. **Figure 2a** displays the structure of the PSC with the configuration of ITO/SnO_2/$Cs_{0.1}FA_{0.9}PbI_3$/spiro-MeOTAD/Au, in which the perovskite layer is deposited by RHCVD with a composition of $Cs_{0.1}FA_{0.9}PbI_3$. The small amount of Cs cation is used to improve phase stability of $FAPbI_3$.[22-23] Similar to the regular HCVD process, the RHCVD process is a two-step process with the first step consisting of co-evaporation of CsI and PbI_2 by optimizing deposition rates to realize the desired composition.[5, 15] In the second step, the substrates pre-coated with the mixture film of CsI and PbI_2 are placed in a CVD tube furnace to react with FAI to form perovskite. On the basis of the temperature profile (for the heating zone containing the substrates) as a function of time shown in **Figure 2b**, in a regular HCVD process the total deposition time of FAI is approximately 230 min (the temperature ramping time is 65 min and the deposition time is 160 min, and about 5 min cooling when the furnace cap is opened to speed up cooling to lower than 100 °C) to ensure the complete conversion of PbI_2 to perovskite.[15, 19-20] The temperature profile for the heating zone containing organic

precursor is shown in **Figure S1**. The temperature ramping rate is slow, e.g., 2.3 °C/min to obtain stable ramping for a relatively low annealing temperature. Setting higher ramping rates (e.g., 5 °C/min) can lead to uncontrollable temperature fluctuations. For example, when the fast temperature ramping is used, the actual temperature in the CVD tube can reach much higher temperatures than the programmed temperature (**Figure S2**), which may lead to damage in perovskites. We developed a single zone RHCVD process using a rapid-thermal annealing (RTA) tube furnace. The RTA tube furnace uses an infrared (IR) heating component to achieve ultrafast temperature ramping. The IR heating component is mechanically movable along the furnace tube, which enables fast heating and cooling. The RHCVD process for the deposition of perovskite is less than 10 min (**Figure 2b**). Detailed steps of the RHCVD process for the deposition of perovskite films are depicted in **Figure 1**. Although a similar process was reported previously for the growth of graphene[24], our work is the first report to apply this process for fabrication of PSCs.

The as-deposited $Cs_{0.1}FA_{0.9}PbI_3$ film shows a smooth surface and grain size in the range of 300-500 nm (**Figure 2c**). SEM micrographs confirm the good uniformity of the surface morphology of the RHCVD deposited perovskite films across a relatively large area (20 μm × 13 μm) (**Figure S3**). The XRD result confirms the full conversion of PbI_2 to perovskite as there is a strong peak at 14.0° and no observable peak at 12.7° (**Figure 2d**). The smooth baseline and the absence of the peak at around 11.6° indicate that the formed perovskite film is mainly pure α-phase. High resolution Cs 3d core-level X-ray photoelectron spectroscopy (XPS) data verify the incorporation of Cs cations into perovskite (**Figure S4**), which agrees well with our previous study on the $Cs_{0.1}FA_{0.9}PbI_{2.9}Br_{0.1}$ perovskite film prepared by the regular HCVD method.[15] The composition ratio between Cs and Pb is determined by XPS to be approximately 1:10, which agrees well with the desired ratio. Our previous mass spectrometry

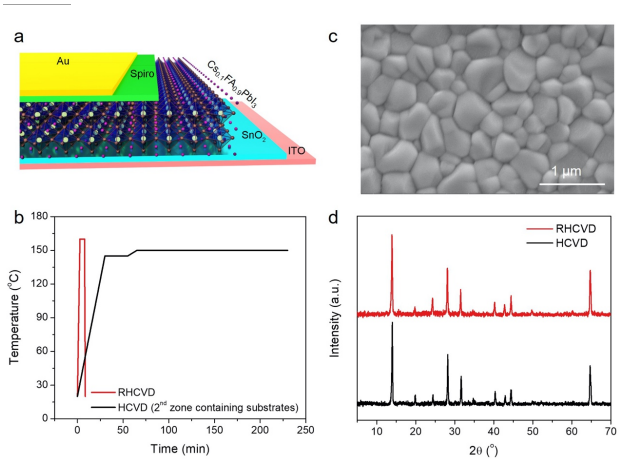

Figure 2. a. Schematic drawing showing the RHCVD PSC structure. **b.** Programmed temperature profile as a function of time during RHCVD and the regular HCVD process for the heating zone containing the substrates. **c.** SEM image of perovskite processed by RHCVD. **d.** XRD pattern of the RHCVD perovskite film.

studies suggest that iodide (I^-) can easily desorb from iodide-based perovskite films leading to iodine (I_2) gas generation under vacuum conditions.[25-26] In the HCVD or RHCVD processes, the large amount of the organic precursor FAI in the crucible (0.1 g) provides the sufficient supply of I^- minimizing the deterioration of perovskite films during the RHCVD process. Furthermore, the fact that perovskite films prepared by RHCVD show high quality and uniformity over a large area (even without additional annealing as compared to most solution processed perovskite films) indicates that RHCVD is an efficient way to form perovskite films, possibly thanks to the dual function of IR heating in promoting perovskite formation as well as uniformly heating the converted perovskite films to enhance their crystallinity. The electronic structures of the deposited perovskite $Cs_{0.1}FA_{0.9}PbI_3$ film has been further investigated by UPS (**Figure S5**). The deposited perovskite showed an n-type nature with a work function of 3.92 eV and valance band maximum of 1.50 eV below the Fermi level. The absorbance of the perovskite has been characterized by UV-vis and the optical band gap of 1.56 eV is extracted from the tauc-plot (**Figure S6**).

Our solar cells are based on the perovskite films deposited by RHCVD and the SnO_2 ETL. In our previous work, the SnO_2 ETL was fabricated by sputtering at room temperature.[27] The crystallinity of the sputtered SnO_2 films was studied as a function of post-annealing temperature in the range of 100-500 °C. The room temperature deposited SnO_2 film showed an amorphous structure, and the crystallinity was only observed after post-annealing at temperatures over 300 °C.[27] However, the post-annealing process also deteriorated the quality of the SnO_2 films.[27] Similarly to the reports of Park and coworkers that annealing of the amorphous SnO_2 ETL to 500 °C crystalize SnO_2. However, the enhanced crystallinity reduced the device performance and led to large hysteresis, due to the increased interface capacitance.[28] Furthermore, the vacuum annealing process during the regular HCVD process not only damages the deposited SnO_2 films, but also increases the density of gap states located between the valance band and Fermi level, which might further decrease the as-prepared devices.[15] On the other hand, solution processed films using SnO_2 nanocrystal solutions exhibit a higher quality compared with sputtered amorphous SnO_2 films after the similar vacuum annealing process in a CVD tube furnace.[15] In this work, we performed a detailed study to investigate the influence of the sputtered amorphous SnO_2 (i.e., without post-annealing to avoid the damage) and thoroughly studied solution-processed SnO_2 films on the PSCs device performance.[29-30] First, the nanocrystal SnO_2 layer was prepared by spin coating, or alternately, an amorphous SnO_2 layer was prepared by sputtering coating on the ITO/glass substrates. The surface morphology of the SnO_2 film was first characterized by atomic force microscopy (AFM). As can be seen in **Figure S7**, the solution processed nano-crystal SnO_2 film shows a smoother morphology compared with the sputtered SnO_2 film. The surface roughness (RMS) for the sputtered SnO_2 and solution coated nanocrystal SnO_2 film is 2.79 and 0.88 nm, respectively (**Figure S7**). The RMS of sputtered amorphous SnO_2 layer is similar to the ITO substrates of 2.45 nm due to a

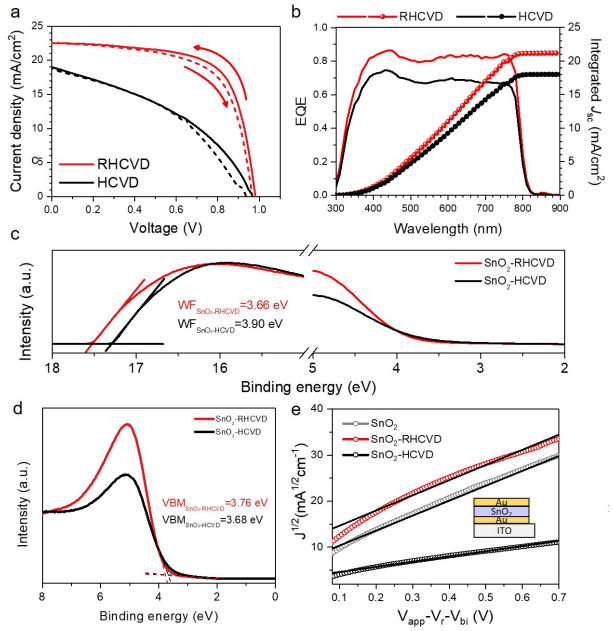

Figure 3. a. J-V curves of the champion PSCs based on RHCVD and the regular HCVD process with the forward and reverse scan. **b.** IPCE spectra of the champion PSC based on RHCVD and the regular HCVD process. **c.** UPS spectra of the SnO_2 films treated under the RHCVD process and the regular HCVD process. **d.** Enlarged UPS valence features of the SnO_2 films based on the RHCVD process and the regular HCVD process. **e.** Electron mobility for the as-prepared SnO_2 film, the SnO_2 film after treatment of the RHCVD process and the regular HCVD process using the SCLC method. The device structure of ITO/Au/SnO_2/Au is shown as the inset.

conformal coating, while the SnO_2 nanocrystals help reduce the surface roughness of the substrate.[27]

The PCE for the PSC device based on the spin coated SnO_2 nanocrystals ETL is 15.0% in the reverse scan and 14.1% in the forward scan (**Figure S8**). Comparing the PCEs from the reverse scans, the PSC devices have negligible differences based on solution coated SnO_2 and sputter deposited SnO_2. However, the PSC devices with sputter-deposited SnO_2 ETL showed 7 times higher hysteresis index (0.06 versus 0.41; hysteresis index = $(PCE_{reverse} - PCE_{forward})/PCE_{reverse}$) and 57.4% lower forward scan efficiency. The severe hysteresis issue in PSC devices can be attributed to the sputtered SnO_2 ETL that has combination of the amorphous structure, high surface roughness and a large defect density.[27-29] Hence, we selected solution coated SnO_2 nanocrystals film as ETL to fabricate subsequent PSC devices.

We have further studied the advantages of RHCVD compared with the regular HCVD process. The most significant advantage is the much shorter deposition time thanks to the rapid thermal process. RHCVD can lead to increase throughput and hence lower cost. It also eliminates the long-time vacuum annealing effect on the SnO_2 ETL.[15] **Figure 3a** compares the representative J-V curves for the PSC devices fabricated based on RHCVD and regular HCVD. Similar to our previous study, the long-time vacuum annealing process in the regular HCVD process deteriorates the quality of the SnO_2 ETL, and the PSC device performance is much lower. The photovoltaic parameters are summarized in **Table 1**. For RHCVD, the champion PSC device shows a PCE of 15.5%. In contrast, for regular HCVD, the PCE is only approximately 7.6%. Although the addition of a thin layer of C_{60} and formation of a SnO_2/C_{60} double-layer ETL could help improve the PSC performance as reported in our previous work,[15] this additional step of vacuum deposition of C_{60} will increase complexity of the fabrication and increase the LCOE. For RHCVD, because the high-quality of the SnO_2 ETL is maintained during the much shorter vacuum annealing process, the PSC device performance is much higher. PSC devices fabricated via a regular HCVD process show lower current density, and the incident-photon-to-current-efficiency (IPCE) spectra (**Figure 3b**) confirm the results obtained from the J-V curves (**Table 1**). The current density of the perovskite cell fabricated from RHCVD process was determined to be 22.3 mA/cm^2 from the J-V curve and 21.2 mA/cm^2 from the EQE curve (4.93% difference), and that of the perovskite solar cell fabricated from regular HCVD was determined to be 18.8 mA/cm^2 from the J-V curve and 18.0 mA/cm^2 from the EQE curve (4.26% difference). Although these differences are not negligible, they are within a relatively low level (i.e., below 5% of the current density) (see **Table S1**), which suggests that our measurements were reasonably accurate.[31] The optical properties of the SnO_2 films after treatment of the RHCVD process and the regular HCVD process have been characterized

Table 1. Photovoltaic parameters for PSCs using the RHCVD process and the regular HCVD process.

		Scan direction	V_{OC} (V)	J_{SC} (mA/cm^2)	FF (%)	PCE (%)
RHCVD	Champion	Reverse	0.99	22.3	70.2	15.5
		Forward	0.97	22.6	64.5	14.1
	Average	Reverse	0.98±0.01	22.2±0.4	65.8±3.5	14.3±0.8
		Forward	0.96±0.02	22.3±0.4	63.9±1.9	13.9±0.6
Regular HCVD	Champion	Reverse	0.96	19.0	42.1	7.6
		Forward	0.93	18.8	40.0	7.0
	Average	Reverse	0.91±0.05	17.5±1.0	43.9±1.4	7.0±0.3
		Forward	0.93±0.04	17.5±1.2	42.4±1.7	6.8±0.3

Table 2. The major differences between the previous work (*J. Mater. Chem. A* **2019**, *7*, 6920-6929) and the current work.

	J. Mater. Chem. A 2019, 7, 6920-6929.	This work
Deposition time	A total of 230 min (including the ramping, deposition and cooling).	Less than 10 min with a rapid ramping and deposition process.
The heating component	In the regular HCVD process, the tube furnace is heated by resistive heating (i.e., using filaments); the ramping of the temperature is slow and temperature fluctuation is large.	For the RHCVD process, we use a rapid-thermal annealing tube furnace, which uses an infrared (IR) heating component with stable control of temperature. The IR heating component is mechanically movable along the furnace tube, which enables fast heating and cooling. This is the first report to apply this rapid thermal annealing process for fabrication of PSCs and PSMs.
ETL structure	The SnO_2 ETL was deposited by sputtering process in room temperature and it is amorphous structure. Due to the prolong vacuum annealing process, the SnO_2 quality has been reduced with increased gap states. A thin layer of C_{60} has been incorporated to maintain the electron extraction and transport properties. However, this complicated the deposition process with one more vacuum deposition step.	In this work the SnO_2 ETL was prepared using a solution of SnO_2 nano-crystals.
Hysteresis and device performance	Due to the prolong vacuum annealing process and induced gap states in ETL SnO_2, the solar cells and modules showed hysteresis. And modules with 22.4 cm^2 designated area showed a PCE of 10%, with 91.8 cm^2 designated area showed a PCE of 9.34%.	In the case of RHCVD, the solar cells and modules showed substantially reduced hysteresis with the high quality SnO_2. PSMs with a designated area of 22.4 cm^2 showed a PCE of 12.3%.
Operational stability	The T_{80} lifetime is around 500 h.	The T_{90} lifetime is over 800 h. The much better operation stability is most likely due to the higher quality of the SnO_2 ETL, i.e., the new RHCVD method leads to a lower density of gap states in the SnO_2 ETL.

(**Figure S9**). As shown in **Figure S9**, the transmittance of both films on quartz substrate is similar to each, and the optical band gap of both films extracted from tauc-plot is 3.85 eV. This large band gap is expected to show a deep valance band and suitable hole blocking properties.

We further study the defect density of the SnO_2 films that experienced different vacuum annealing processes to understand their influence on the PSC device performance. Ultraviolet photoemission spectroscopy (UPS) and XPS measurements were carried out to characterize the surface properties of the SnO_2 films after the vacuum annealing process. To understand the surface properties, SnO_2 films coated on ITO substrates were placed into the CVD tube furnace to simulate the vacuum annealing process during RHCVD and regular HCVD. No organic precursors were loaded into the CVD furnace for the study of the effects of temperature and vacuum conditions. As shown in **Figure 3c**, the SnO_2 film that experienced the RHCVD vacuum annealing process shows a lower work function (WF) of 3.66 eV. While for the SnO_2 film that experienced the regular HCVD vacuum annealing process the WF is much higher (3.90 eV). As the ETL layer, a lower WF is expected to better facilitate electron extraction.[32-33] This explains why the PSC devices based on the SnO_2 ETL that experienced long vacuum annealing showed the poorer performance. The gap state density between the valance band minimum and the Fermi level also increases for the longer vacuum annealing process (**Figure 3c**).[15] The enlarged UPS valence features (**Figure 3d**) and high

resolution XPS valance feature (**Figure S10**) further confirm the increased gap states between the valance band and the Fermi level. These gap states lower the hole blocking barrier and increase recombination, hence lower the V_{OC} and the PCE of the PSCs.[27] We used the space-charge limited-current (SCLC) technique to characterize the electronic properties of the devices based on the symmetric sandwich structure (see the inset in **Figure 3e**). The mobility was calculated using the Mott–Gurney law.[34] The mobility for the freshly coated SnO_2 film was 5.0×10^{-4} cm^2 V^{-1} s^{-1}. After the short vacuum annealing process (10 min) to simulate the RHCVD process, the mobility of the SnO_2 film became 5.1×10^{-4} cm^2 V^{-1} s^{-1}, which was almost the same as before. However, the mobility for the SnO_2 film that experienced a longer vacuum annealing process of 230 min showed a much lower mobility of 1.7×10^{-4} cm^2 V^{-1} s^{-1}, which is likely the result of the increased gap states acting as scattering/trapping centres. These observations strongly suggest that RHCVD not only significantly reduces the deposition time, but also maintains the high quality of the SnO_2 nanocrystals ETL, which is the main reason for PCE to increase up to 15.5%.

To help understand the main reason responsible for the current density reduction, we studied the energy level alignment based on perovskite and SnO_2 for the case of RHCVD versus regular HCVD (**Figure S11**). Similar to previous reports on planar solar cells based on SnO_2 and TiO_2 ETL, the energy level mismatch at the perovskite/TiO_2 interface prevents efficient charge extraction and therefore leads to reduced current density.[35-39] Here in this work, the conduction band of the SnO_2 film that experienced the regular HCVD process shows a upward shift; and work function also increases by 0.24 eV. There is an energy barrier for electron extraction from perovskite to SnO_2. For the SnO_2 film that experienced the RHCVD process, the energy level alignment between perovskite and SnO_2 is better (**Figure S11**). The low work function helps facilitate electron extraction. Furthermore, with a prolonged vacuum annealing during the regular HCVD process, more gap states appear above the valance band of the SnO_2 film, which lowers the hole blocking properties of this interface and increases charge carrier recombination (**Figure S11**).[27]

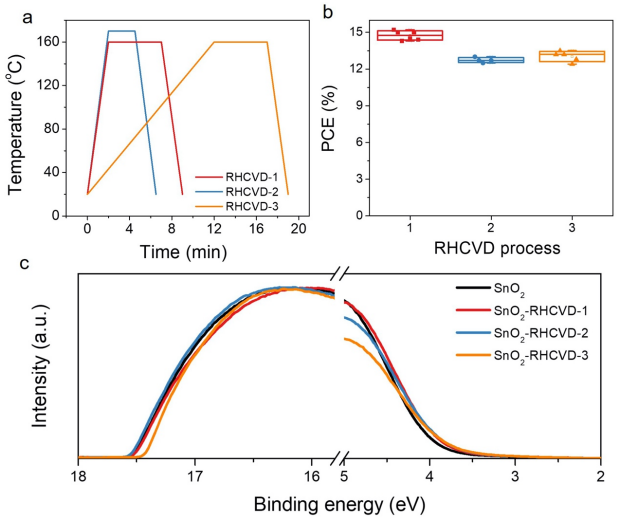

Figure 4. a. Temperature profile as a function of time during different RHCVD processes. The RHCVD-2 process has a higher temperature and a shorter treatment time compared with the RHCVD-1 process. The RHCVD-3 process has a slower ramping rate during temperature increase compared with the RHCVD-1 process. **b.** The dependence of PCE on different RHCVD processes. **c.** UPS spectra of the SnO_2 films treated with different RHCVD processes.

To further verify that vacuum annealing deteriorates charge carrier extraction and increases charge carrier recombination, we fabricated solar cells based on solution coated perovskite films deposited on SnO_2 ETL with and without vacuum annealing, and the results are shown in **Figure S12**. As we can see, the solar cell device based on the SnO_2 ETL film after a long time of vacuum annealing shows lower performance with reduced open circuit voltage, short circuit current density and fill factor, which is similar to our previous results.[15] On the other hand, the solar cell device based on the SnO_2 ETL film after a short time of vacuum annealing as in the RHCVD process does not show much difference between the control sample case and the RHCVD-treated SnO_2 case. The faster carrier extraction of perovskite films to the SnO_2 films after treatment of the RHCVD process has been further verified by the time resolved photoluminescent (TRPL) spectra (**Figure S13** and **Table S2**). The resulting curves are fitted by a double exponential model with a fast and slow decay time constants (τ_1 and τ_2).[36] The fast decay time constant τ_1 corresponds to the quenching of charge carriers by electron extraction from $CH_3NH_3PbI_3$ to SnO_2.[27] With the reduced vacuum annealing process time, the fast time constant τ_1 decreased from 17.8 ns for $CH_3NH_3PbI_3$ on SnO_2-HCVD to 10.9 ns for $CH_3NH_3PbI_3$ on SnO_2-RHCVD. This observation also implies that a longer vacuum annealing process may increase the gap states and deteriorate the quality of the SnO_2 layer.

In the case of regular HCVD, the combination of mismatched energy levels between the SnO_2 ETL and the perovskite film, increased gap states in the SnO_2 ETL, and reduced mobility of the SnO_2 film contributed to the decreased solar cell performance. Furthermore, the major differences between the regular HCVD and RHCVD have been summarized in **Table 2**.

The balance between the temperature ramping time, deposition time and perovskite layer thickness has been studied to further optimize the RHCVD process. Higher temperatures can shorten the deposition time. However, the deposition rate of FAI and the reaction between deposited FAI and PbI_2 need be balanced. If FAI is deposited faster than its reaction with PbI_2, there will be excess FAI on top of the perovskite film. When FAI is deposited slower than its reaction with PbI_2, the feeding of FAI will be the time determining step and a longer time is required for the complete conversion of PbI_2 to perovskite. The optimized condition for RHCVD corresponds to a balanced condition required for vaporization of FAI, diffusion into PbI_2 and reaction with PbI_2.[15, 40] Upon temperature increase, both

the FAI deposition rate and the reaction rate with PbI_2 increase. As the temperature increased to 170 °C (RHCVD-2 in **Figure 4a**), the device performance started to decrease (**Figure 4b**), which indicates a faster increase of the FAI deposition rate compared with its reaction rate with PbI_2, and a pale surface on the top of the perovskite film was observed after being taken out from the tube. On the other hand, with a slower ramping rate (RHCVD-3 in **Figure 4a**), the total vacuum annealing time will increase, and the WF of the SnO_2 ETL prepared from SnO_2 nanocrystal rises slightly (**Figure 4c**). Based on this, a shorter reaction time and higher ramping rate benefit the formation of high-quality perovskite films and SnO_2 film. The thickness of the PbI_2 film also influences the deposition time because a thicker PbI_2 film would need more FAI for the conversion to perovskite. To ensure sufficient light absorbance, a thickness of 370 nm for the perovskite was chosen in this work (**Figure S14**).[5]

HCVD is promising for upscalable fabrication of PSCs. 10 cm × 10 cm PSMs have been demonstrated for the regular HCVD process and the upscaling of the size from 0.1 cm^2 to 91.8 cm^2 shows a small absolute PCE decay rate of 1.3%/decade area.[15] Similarly, in this work we also tested upscalable capability of RHCVD. Here the CVD tube furnace used for the RHCVD process has an inner diameter of 96 mm, which is the only limitation for the size of the substrates to be used. We fabricated a PSM on a 5 cm × 5 cm substrate using the RHCVD process. The PSM has a designated area of 22.4 cm^2 with 7 cells connected in series. For each subcell the ITO stripe width is 6.6 mm, and there is a 0.1 mm P1 patterning line between each sub stripe. The length of each sub-cell is 4.8 cm, with 1 mm space at the edges that are perpendicular to the patterning lines. The edges that are parallel to the patterning line have a space of 1.6 mm and are used for wiring of the electrodes (**Figure S15**). The typical geometric fill factor for the module is approximately 90%.[15, 27] The champion PSM has a PCE of 12.3% and almost no hysteresis (**Figure 5a, b**). Furthermore, the continuous operation of the PSM under continuous light illumination in a dry N_2 box has been measured by recording the PSM power output under a steady voltage output, which corresponds to the initial maximum power point voltage. As shown in **Figure 5c**, the power output of the PSM maintains 90% of its initial value after continuous working under light illumination after 800 h. The RHCVD process shows a significantly shorter processing time and longer operation stability and is a promising method for upscalable fabrication of PSMs with larger areas, smaller PCE decay and longer operational lifetime (**Table S3**).

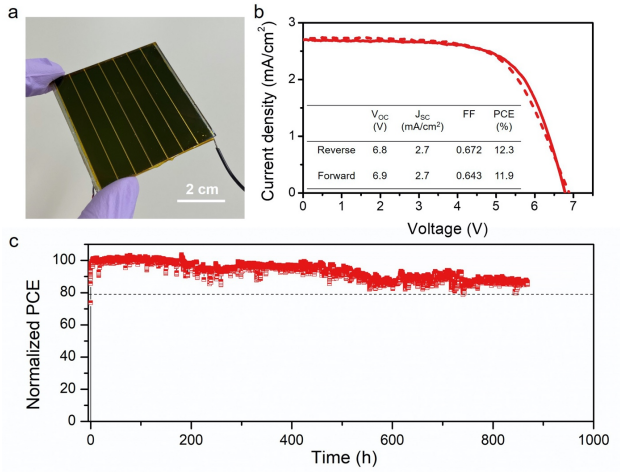

Figure 5. PSMs fabricated by the RHCVD process. **a.** Photograph of a 5 cm × 5 cm PSM. **b.** Forward scan and reverse scan of the PSM with the best performance of 12.3%. **c.** Continuous operation of PSMs under continuous light illumination.

Experiment

Materials. All the commercial materials were used as received without further purification, including SnO_2 (Alfa Aesar, tin (IV) oxide, 15% in H_2O colloidal dispersion), PbI_2 (99.99%, TCI), CsI (99.99% Sigma), formamidinium iodide (FAI, greatcell solar), isopropanol (Wako), 2,2',7,7'-tetrakis (N, N-di-p-methoxyphenylamine)-9,9'-spirobifluorene (spiro-MeOTAD, Merck).

Solar cell devices fabrication. Indium-doped tin oxide (ITO) substrates were washed with distilled water, acetone and isopropanol in sequential, and dried with N_2 gas. Before the usage of the ITO substrates, they were pre-treated under UV/O_3 for 30 min. The SnO_2 layer was coated on the ITO surface by spin coating of SnO_2 nanocrystal solution (2.5% in distilled water) at 3000 rpm for 30 s, followed by drying at 150 °C for 30 min. The perovskite precursor layer was deposited by a thermal co-evaporation process of PbI_2 and CsI, which was reported in our previous work.[15] Here the evaporation rate of PbI_2 and CsI was controlled to be 0.10 nm/s and 0.01 nm/s, respectively. Then the PbI_2/CsI coated substrate was transferred to a single-zone tube or a multi-zone tube furnace to conduct the RHCVD process or the regular HCVD process. After reaction and cooling, the resultant perovskite film was washed with IPA solution, followed by heating at 100 °C for 20 min to remove the residual FAI in the surface of perovskite. A hole transport material solution was spin-coated on the top of the perovskite layer at the rotation speed of 3000 rpm for 30 s. The hole transport material solution contained 29 mg spiro-MeOTAD, 11.5 μL TBP and 7 μL Li-TFSI solution in 0.4 mL chlorobenzene. Finally, a layer of 100 nm thickness of gold was evaporated as the back-contact electrode. For module fabrication, the Au electrode thickness was 120 nm.

RHCVD. Detailed steps of RHCVD process for the deposition of perovskite films are depicted in **Figure 1**. In brief, the RHCVD process is performed in a single-zone tube furnace with FAI powder as the precursor. At one end of the tube furnace a vacuum pump is connected, and at the other end a vacuum gauge is connected and controls the vacuum level of the furnace to 10 Torr. During the RHCVD process, a sufficient amount of FAI powder (0.1 g) is placed in the upstream zone of the furnace close to the pre-deposited CsI/PbI_2 substrate. After the reaction,

the furnace is moved and the heating zone is cooled with a fan to accelerate the cooling speed of the tube.

Characterization. Surface morphology was observed using an SEM (FEI Quanta 250 FEG). The UPS and XPS spectra were recorded using an XPS-AXIS Ultra HAS (Kratos) with monochromatic Al-Kα=1486.6 eV and non-monochromatic He-Iα=21.22 eV sources. The crystal structure of the perovskite was analysed using an XRD (Bruker D8 Discover). J-V curves of the solar cells were measured using a Keithley 2420 Source Meter under AM1.5 illumination generated from a solar simulator (Oriel-Sol3A). The illumination intensity of 100 mW/cm^2 was adjusted by using a reference silicon solar cell before the measurements on PSCs and PSMs.

Conclusions

HCVD is promising for upscalable fabrication of PSMs. The significant reduction in the processing time from hours to tens of minutes is important to further increase production throughput of PSMs by HCVD. Here in this work, we developed a RHCVD process, which helps maintain the high-quality SnO_2 ETL and deposition of high-quality perovskite layers. With the optimization of various parameters for the RHCVD fabrication (e.g., process temperature, perovskite layer thickness, SnO_2 ETL, etc.), PSCs with PCEs up to 15.5% and PSMs with a PCE of 12.3% have been demonstrated. The fabrication of PSMs shows the upscalable capability of this RHCVD process. Furthermore, the fabricated PSM shows a high operational lifetime which maintains 90% of its initial value after 800 hours continues working under light illumination at a steady state.

Conflicts of interest

Yabing Qi, Longbin Qiu, Sisi He, and Luis K. Ono are named inventors on the patent application 63036068 (filing date June 8, 2020), which is related to the techniques described in this article.

Acknowledgements

This work was supported by funding from the Energy Materials and Surface Sciences Unit of the Okinawa Institute of Science and Technology Graduate University, the OIST Proof of Concept (POC) Program, and the OIST R&D Cluster Research Program. We thank OIST Mech. Eng. & Microfabrication Support Section for maintenance of cleanroom and the OIST Imaging Section for support.

References

1 Green, M. A.; Dunlop, E. D.; Hohl-Ebinger, J.; Yoshita, M.; Kopidakis, N., Ho-Baillie, A. W. Y. Solar cell efficiency tables (Version 55). *Prog. Photovolt. Res. Appl.* **2020**, *28*, 3-15.

2 Cai, M.; Wu, Y.; Chen, H.; Yang, X.; Qiang, Y., Han, L. Cost-Performance Analysis of Perovskite Solar Modules. *Adv. Sci.* **2017**, *4*, 1600269.

3 He, S.; Qiu, L.; Ono, L. K., Qi, Y. B. How far are we from attaining 10-year lifetime for metal halide perovskite solar cells? *Mater. Sci. Eng. R Rep.* **2020**, *140*, 100545.

4 Chu, S.; Cui, Y., Liu, N. The path towards sustainable energy. *Nat. Mater.* **2017**, *16*, 16-22.

5 Qiu, L.; He, S.; Ono, L. K.; Liu, S., Qi, Y. B. Scalable Fabrication of Metal Halide Perovskite Solar Cells and Modules. *ACS Energy Lett.* **2019**, *4*, 2147-2167.

6 Li, Z.; Klein, T. R.; Kim, D. H.; Yang, M.; Berry, J. J.; van Hest, M. F. A. M., Zhu, K. Scalable fabrication of perovskite solar cells. *Nat. Rev. Mater.* **2018**, *3*, 18017.

7 Park, N.-G., Zhu, K. Scalable fabrication and coating methods for perovskite solar cells and solar modules. *Nat. Rev. Mater.* **2020**, *5*, 333-350.

8 Dai, X.; Deng, Y.; Van Brackle, C. H.; Chen, S.; Rudd, P. N.; Xiao, X.; Lin, Y.; Chen, B., Huang, J. Scalable Fabrication of Efficient Perovskite Solar Modules on Flexible Glass Substrates. *Adv. Energy Mater.* **2020**, *10*, 1903108.

9 Yang, M.; Kim, D. H.; Klein, T. R.; Li, Z.; Reese, M. O.; Tremolet de Villers, B. J.; Berry, J. J.; van Hest, M. F. A. M., Zhu, K. Highly Efficient Perovskite Solar Modules by Scalable Fabrication and Interconnection Optimization. *ACS Energy Lett.* **2018**, *3*, 322-328.

10 Patidar, R.; Burkitt, D.; Hooper, K.; Richards, D., Watson, T. Slot-die coating of perovskite solar cells: An overview. *Mater. Today Commun.* **2020**, *22*, 100808.

11 Remeika, M.; Raga, S. R.; Zhang, S., Qi, Y. B. Transferrable optimization of spray-coated PbI_2 films for perovskite solar cell fabrication. *J. Mater. Chem. A* **2017**, *5*, 5709-5718.

12 Gil-Escrig, L.; Momblona, C.; La-Placa, M.-G.; Boix, P. P.; Sessolo, M., Bolink, H. J. Vacuum Deposited Triple-Cation Mixed-Halide Perovskite Solar Cells. *Adv. Energy Mater.* **2018**, *8*, 1703506.

13 Jiang, Y.; Remeika, M.; Hu, Z.; Juarez-Perez, E. J.; Qiu, L.; Liu, Z.; Kim, T.; Ono, L. K.; Son, D.-Y.; Hawash, Z.; Leyden, M. R.; Wu, Z.; Meng, L.; Hu, J., Qi, Y. B. Negligible-Pb-Waste and Upscalable Perovskite Deposition Technology for High-Operational-Stability Perovskite Solar Modules. *Adv. Energy Mater.* **2019**, *9*, 1803047.

14 Leyden, M. R.; Ono, L. K.; Raga, S. R.; Kato, Y.; Wang, S., Qi, Y. B. High performance perovskite solar cells by hybrid chemical vapor deposition. *J. Mater. Chem. A* **2014**, *2*, 18742-18745.

15 Qiu, L.; He, S.; Jiang, Y.; Son, D.-Y.; Ono, L. K.; Liu, Z.; Kim, T.; Bouloumis, T.; Kazaoui, S., Qi, Y. B. Hybrid chemical vapor deposition enables scalable and stable Cs-FA mixed cation perovskite solar modules with a designated area of 91.8 cm^2 approaching 10% efficiency. *J. Mater. Chem. A* **2019**, *7*, 6920-6929.

16 Yin, J.; Qu, H.; Cao, J.; Tai, H.; Li, J., Zheng, N. Vapor-assisted crystallization control toward high performance perovskite photovoltaics with over 18% efficiency in the ambient atmosphere. *J. Mater. Chem. A* **2016**, *4*, 13203-13210.

17 Tavakoli, M. M.; Zakeeruddin, S. M.; Grätzel, M., Fan, Z. Large-Grain Tin-Rich Perovskite Films for Efficient Solar Cells via Metal Alloying Technique. *Adv. Mater.* **2018**, *30*, 1705998.

18 Tavakoli, M. M.; Gu, L.; Gao, Y.; Reckmeier, C.; He, J.; Rogach, A. L.; Yao, Y., Fan, Z. Fabrication of efficient planar perovskite solar cells using a one-step chemical vapor deposition method. *Sci. Rep.* **2015**, *5*, 14083.

19 Li, M.-H.; Yeh, H.-H.; Chiang, Y.-H.; Jeng, U.-S.; Su, C.-J.; Shiu, H.-W.; Hsu, Y.-J.; Kosugi, N.; Ohigashi, T.; Chen, Y.-A.; Shen, P.-S.; Chen, P., Guo, T.-F. Highly Efficient 2D/3D Hybrid Perovskite Solar Cells via Low-Pressure Vapor-Assisted Solution Process. *Adv. Mater.* **2018**, *30*, 1801401.

20 Luo, L.; Zhang, Y.; Chai, N.; Deng, X.; Zhong, J.; Huang, F.; Peng, Y.; Ku, Z., Cheng, Y.-B. Large-area perovskite solar cells with $Cs_xFA_{1-x}PbI_{3-y}Br_y$ thin films deposited by a vapor–solid reaction method. *J. Mater. Chem. A* **2018**, *6*, 21143-21148.

21 Kim, J. H.; Liang, P.-W.; Williams, S. T.; Cho, N.; Chueh, C.-C.; Glaz, M. S.; Ginger, D. S., Jen, A. K.-Y. High-Performance and Environmentally Stable Planar Heterojunction Perovskite Solar Cells Based on a Solution-Processed Copper-Doped Nickel Oxide Hole-Transporting Layer. *Adv. Mater.* **2015**, *27*, 695-701.

22 Turren-Cruz, S.-H.; Hagfeldt, A., Saliba, M. Methylammonium-free, high-performance, and stable perovskite solar cells on a planar architecture. *Science* **2018**, *362*, 449-453.

23 Jiang, Y.; Leyden, M. R.; Qiu, L.; Wang, S.; Ono, L. K.; Wu, Z.; Juarez-Perez, E. J., Qi, Y. B. Combination of Hybrid CVD and Cation Exchange for Upscaling Cs-Substituted Mixed Cation Perovskite Solar Cells with High Efficiency and Stability. *Adv. Funct. Mater.* **2018**, *28*, 1703835.

24 Xiong, W.; Zhou, Y. S.; Jiang, L. J.; Sarkar, A.; Mahjouri-Samani, M.; Xie, Z. Q.; Gao, Y.; Ianno, N. J.; Jiang, L., Lu, Y. F. Single-Step Formation of Graphene on Dielectric Surfaces. *Adv. Mater.* **2013**, *25*, 630-634.

25 Juarez-Perez, E. J.; Hawash, Z.; Raga, S. R.; Ono, L. K., Qi, Y. B. Thermal degradation of $CH_3NH_3PbI_3$ perovskite into NH_3 and CH_3I gases observed by coupled thermogravimetry–mass spectrometry analysis. *Energy Environ. Sci.* **2016**, *9*, 3406-3410.

26 Juarez-Perez, E. J.; Ono, L. K.; Maeda, M.; Jiang, Y.; Hawash, Z., Qi, Y. B. Photodecomposition and thermal decomposition in methylammonium halide lead perovskites and inferred design principles to increase photovoltaic device stability. *J. Mater. Chem. A* **2018**, *6*, 9604-9612.

27 Qiu, L.; Liu, Z.; Ono, L. K.; Jiang, Y.; Son, D.-Y.; Hawash, Z.; He, S., Qi, Y. B. Scalable Fabrication of Stable High Efficiency Perovskite Solar Cells and Modules Utilizing Room Temperature Sputtered SnO_2 Electron Transport Layer. *Adv. Funct. Mater.* **2019**, *29*, 1806779.

28 Jung, K.-H., Seo, J.-Y., Lee, S., Shin, H. and Park, N.-G. Solution-processed SnO_2 thin film for a hysteresis-free planar perovskite solar cell with a power conversion efficiency of 19.2%. *J. Mater. Chem. A* **2017**, *5*, 24790-24803.

29 Jiang, Q.; Zhang, L.; Wang, H.; Yang, X.; Meng, J.; Liu, H.; Yin, Z.; Wu, J.; Zhang, X., You, J. Enhanced electron extraction using SnO_2 for high-efficiency planar-structure $HC(NH_2)_2PbI_3$-based perovskite solar cells. *Nat. Energy* **2016**, *2*, 16177.

30 Jiang, Q.; Zhang, X., You, J. SnO_2: A Wonderful Electron Transport Layer for Perovskite Solar Cells. *Small* **2018**, 14, 1801154.

31 Saliba, M. and Etgar, L. Current Density Mismatch in Perovskite Solar Cells. *ACS Energy Lett.* **2020**, *5*, 2886-2888.

32 Zhou, Y.; Fuentes-Hernandez, C.; Shim, J.; Meyer, J.; Giordano, A. J.; Li, H.; Winget, P.; Papadopoulos, T.; Cheun, H.; Kim, J.; Fenoll, M.; Dindar, A.; Haske, W.; Najafabadi, E.; Khan, T. M.; Sojoudi, H.; Barlow, S.; Graham, S.; Brédas, J.-L.; Marder, S. R.; Kahn, A., Kippelen, B. A Universal Method to Produce Low–Work Function Electrodes for Organic Electronics. *Science* **2012**, *336*, 327-332.

33 Qiu, L.; Ono, L. K.; Jiang, Y.; Leyden, M. R.; Raga, S. R.; Wang, S., Qi, Y. B. Engineering Interface Structure to Improve Efficiency and Stability of Organometal Halide Perovskite Solar Cells. *J. Phys. Chem. B* **2018**, *122*, 511-520.

34 Yang, D.; Yang, R.; Wang, K.; Wu, C.; Zhu, X.; Feng, J.; Ren, X.; Fang, G.; Priya, S., Liu, S. High efficiency planar-type perovskite solar cells with negligible hysteresis using EDTA-complexed SnO_2. *Nat. Commun.* **2018**, *9*, 3239.

35 Correa Baena, J. P., Steier, L., Tress, W., Saliba, M., Neutzner, S., Matsui, T., Giordano, F., Jacobsson, T. J., Srimath Kandada, A. R., Zakeeruddin, S. M., Petrozza, A., Abate, A., Nazeeruddin, M. K., Grätzel, M. and Hagfeldt, A. Highly efficient planar perovskite solar cells through band alignment engineering. *Energy Environ. Sci.* **2015**, *8*, 2928-2934.

36 Yu, H., Yeom, H.-I., Lee, J. W., Lee, K., Hwang, D., Yun, J., Ryu, J., Lee, J., Bae, S., Kim, S. K. and Jang, J. Superfast Room‐Temperature Activation of SnO_2 Thin Films via Atmospheric Plasma Oxidation and their Application in Planar Perovskite Photovoltaics. *Adv. Mater.* **2018**, *30*, 1704825.

37 Yang, D., Zhou, X., Yang, R., Yang, Z., Yu, W., Wang, X., Li, C., Liu, S. and Chang, R. P. H. Surface optimization to eliminate hysteresis for record efficiency planar perovskite solar cells. *Energy Environ. Sci.* **2016**, *9*, 3071-3078.

38 Yang, D., Yang, R., Wang, K., Wu, C., Zhu, X., Feng, J., Ren, X., Fang, G., Priya, S. and Liu, S. F. High efficiency planar-type perovskite solar cells with negligible hysteresis using EDTA-complexed SnO_2. *Nat. Commun.* **2018**, *9*, 3239.

39 Liu, Z., Qiu, L., Ono, L. K., He, S., Hu, Z., Jiang, M., Tong, G., Wu, Z., Jiang, Y., Son, D.-Y., Dang, Y., Kazaoui, S. and Qi, Y. B. A holistic approach to interface stabilization for efficient perovskite solar modules with over 2,000-hour operational stability. *Nat. Energy* **2020**, *5*, 596-604.

40 Leyden, M. R.; Lee, M. V.; Raga, S. R., Qi, Y. B. Large formamidinium lead trihalide perovskite solar cells using chemical vapor deposition with high reproducibility and tunable chlorine concentrations. *J. Mater. Chem. A* **2015**, *3*, 16097-16103.